ADVANCED ENERGY MATERIALS
www.advenergymat.de

A New Approach to Fuel Cell Electrodes: Lanthanum Aluminate Yielding Fine Pt Nanoparticle Exsolution for Oxygen Reduction Reaction

*Selda Ozkan, Seo Jin Kim, David N. Miller, and John T. S. Irvine**

Designing an electrocatalyst with low Pt content is an immediate need for essential reactions in low temperature fuel cell systems. In the present work, $La_{0.9925}Ba_{0.0075}Al_{0.995}Pt_{0.005}O_3$ is aimed at using with low (only 0.5%) Pt doping as an electrocatalyst for oxygen reduction reaction (ORR). The low doping level renders exsolution of 1–2 nm nanoparticles with uniform dispersion upon reduction in H_2/N_2 at low temperatures. Pt exsolved perovskite oxides deliver significantly enhanced catalytic activity for ORR and improved stability in alkaline media. This study demonstrates that $LaAlO_3$ with low noble metal content holds immense potential as an electrocatalyst in real fuel cell systems.

1. Introduction

Despite the high cost of Pt, it still remains the strongest (most efficient) electrocatalyst for oxygen reduction reaction (ORR) in acidic and alkaline fuel cells.[1] In recent years, investigations have been focused on lowering the Pt loading and improving the utilization efficiency by enhancing the dispersion of nanoparticles on catalyst support.[2,3] Uniform dispersion of Pt nanoparticles can be achieved by employing traditional and vacuum deposition techniques.[4–7] However, Pt constructed on carbon supports prepared using the aforementioned methods suffers from dissolution, detachment, and agglomeration during fuel cell operation due to structural instability of C and weak interaction/binding between Pt and C.[8] Additionally, the oxidation of the carbon support during the electrocatalytic tests introduces oxygen-containing groups on the support surface, which further weakens the support-particle interaction and increases the electronic resistance.[9,10] As an alternative to unstable, corrosion-prone carbon-based supports, perovskite oxides (ABO_3) are considered owing to their easy tunability of intrinsic and extrinsic properties by doping various metals to either A-site or B-site.[11] Among various perovskite oxides, $LaAlO_3$ exhibits high chemical resistance, high thermal stability, high transparency, high dielectric constant, low toxicity, and good catalytic activity.[12,13] Owing to its surface acidic properties, $LaAlO_3$ has been investigated for various applications, i.e., Imai and Tagawa et al. used it for the oxidative coupling of methane,[14] Wang et al. for the degradation of pollutants,[15] Tran et al. for hydrogenation and dehydrogenation of hydrocarbons[13] and CO_2 methanation,[13] Mukai et al. for steam reforming,[16] Deng et al. for far-infrared radiation applications,[17] Shaik et al. for drug delivery,[18] and Sato et al. for oxidative coupling of methane.[19]

Published studies have reported that A- and B-site substitution of $LaAlO_3$ with various noble and transition metal ions, e.g., A-site with Sr, Ca, Nd,[20–22] and B-site with Rh, Ni, Co, Cu, Ga, Cr, Ce, Mn, Pt, Ru, Pd, changes the electrical, catalytic, optical, and magnetic properties by modifying oxygen vacancy concentration, and valance states of elements.[13,17,23–25] Hashimoto et al. reported that the A-site substitution of $LaAlO_3$, Sr substitution in La-sites, improved oxygen ionic mobility by inducing the formation of oxygen vacancies; on the other hand, A-site deficiency worsened the oxygen ionic conductivity, perovskite oxide behaved like an ionic insulator.[26] For B-site doping, Anil et al. observed improved catalytic activity for the B-site Ru, Pt and Pd (2%) substituted $LaAlO_3$.[25] The main catalytic active sites of perovskite oxides for the ORR are B-site transition metals and oxygen vacancies.[27] The surface oxygen vacancies at moderate level facilitate the conversion of OH_2^- (which is linked to corrosion of the catalyst and reduces the utilization of oxygen) to the desired product of OH^-[28] and improve the electronic, crystal structure, and surface chemistry (active site, surface element composition and OH^- coverage) of perovskite oxides.[27]

Here, to load the catalytically active Pt nanoparticles on the perovskite oxide support, we employed an exsolution process—first incorporating catalytically active component into the B-site of the $LaAlO_3$ perovskite lattice with oxidizing conditions and then released it under a reducing atmosphere.[29,30] In contrast to conventional and vacuum deposition techniques, exsolved nanoparticles can be embedded in the perovskite oxide surface and often form coherent or partially coherent interfaces, this ensures good catalyst-support interaction, direct path for electron transport, high stability, good catalytic activity, and the possibility of regeneration of exsolved nanoparticles under reduction-oxidation

S. Ozkan, S. J. Kim, D. N. Miller, J. T. S. Irvine
School of Chemistry
University of St Andrews
St Andrews KY16 9ST, UK
E-mail: jtsi@st-and.ac.uk

The ORCID identification number(s) for the author(s) of this article can be found under https://doi.org/10.1002/aenm.202303025

DOI: 10.1002/aenm.202303025

cycle.[29,31–34] Furthermore, the exsolution process allows tuning of the particle size, shape, population, composition and induces uniform dispersion by controlling the doping level and process conditions.[35,36]

In the present work, we prepared $La_{0.9925}Ba_{0.0075}Al_{0.995}Pt_{0.005}O_3$ perovskite oxides by solid-state reaction method and induced exsolution of fine Pt nanoparticles during heat treatment in H_2/N_2 at varying, moderate temperatures. The functionalized perovskite oxides were evaluated for ORR in acidic and alkaline media.

2. Result and Discussion

In the present work, Pt-doped $La_{0.9925}Ba_{0.0075}Al_{0.995}Pt_{0.005}O_3$ perovskite oxide was prepared by solid state synthesis, which was subsequently reduced between 400 and 800 °C in 5% H_2/N_2 to promote the exsolution of B-site Pt atoms. We used a low doping level, only 0.5%, due to high cost of noble metals although low levels of doping do also act to minimise the particle clustering.

The grain size of pristine $LaAlO_3$ and Pt-doped $La_{0.9925}Ba_{0.0075}Al_{0.995}Pt_{0.005}O_3$ annealed in 100% O_2 were 120 and 270 nm, respectively (Figures S1 and S2, Supporting Information). The grain size of $LaAlO_3$ is smaller compared to $La_{0.4}Ca_{0.4}TiO_3$ (app. 500–1000 nm) prepared under similar conditions (treatment temperature, duration, ramping rate). In the literature, smaller grain size of perovskite oxides is described as the consequence of the combination of multiple factors, e.g., precursor effect, rare earth oxide (Y_2O_3, La_2O_3, CeO_2) content,[37] annealing temperature (i.e., the grain growth is controlled by grain boundary diffusion and surface diffusion at relatively low temperatures, grain boundary migration, and lattice diffusion at high temperature),[38,39] annealing duration, and precursor concentration. A small grain size of $LaAlO_3$ can be explained by the grain boundary pinning effect of La_2O_3 phase—the presence of La_2O_3 along the grain boundaries prevents boundary migration and suppresses the grain growth.[37,40–43] We observed larger grain size after doping Ba and Pt in $LaAlO_3$ and reduction heat treatment, this could be attributed to the defects and vacancies in the lattice.[44]

We analysed the specific surface area of the perovskite oxide by the Brunauer-Emmet-Teller (BET) method, see Figure S3 (Supporting Information). The BET surface areas of $LaAlO_3$ and LBAPO are fairly low, app. 3.1 and 1.9 $m^2\ g^{-1}$, respectively. The lower surface area of the LBAPO is thought to originate from the high firing temperature of the synthesis method.

Figure 1 illustrates scanning electron microscopy (SEM) and scanning transmission electron microscopy energy dispersive spectroscopy (STEM-EDS) images of 0.5% Pt-$La_{0.9925}Ba_{0.0075}Al_{0.995}O_{3-x}$ reduced at temperatures between 500 and 800 °C. Reduction heat treatment at lower temperatures (between 400 and 700 °C) resulted in no visible Pt particles on the grains when they were analyzed by SEM, as evident in Figure S4 (Supporting Information).

According to the STEM and EDS analysis, reduction at 400 °C does not facilitate egress of Pt particle and STEM-EDS elemental analysis confirms that Pt is still inside the perovskite oxide, see Figure S5 (Supporting Information). The experimental findings indicate that the reduction temperature lower than 500 °C is not sufficient for the emergence of Pt nanoparticles. On the other hand, different from SEM images, STEM images demonstrated the presence of exsolved nanoparticles with the particle size of 1.4 ± 0.9 nm at 500 °C 1.8 ± 0.5 nm at 600 °C and 3.1 ± 0.2 nm at 700 °C, as illustrated in Figure 1; Figure S9 (Supporting Information). The exsolved Pt nanoparticles were spotted on the grains and on the sharp edges of the grains of both fractured and native surfaces. The average Pt nanoparticle size for the sample reduced at 800 °C was ≈9–10 nm from SEM images and 6–7 nm from STEM images. (The size difference is due to the difference in the resolution range of STEM and SEM analysis). From the high-angle annular dark-field (HAADF-STEM) image, the lattice spacing was measured as 2.32 Å assigned to the (111) plane of metallic Pt in face centred cubic (FCC) crystal structure. STEM-EDS analysis of the 0.5%Pt-LBAO R 800 °C confirmed the metallic state of exsolved Pt nanoparticles and uniform distribution of elements (Al, La, Ba, and O) in the perovskite oxides, Figure 1e–e2.

We performed thermogravimetric analysis (TGA) to monitor the mass loss during reduction heat treatment in %5 H_2/N_2 up to 800 °C (data not shown). No significant mass loss indicating exsolution was observed below 600 °C. This finding signifies that the reduction temperature below 600 °C, i.e., 500 °C, resulting in the exsolution of Pt with ≈1-1.4 nm particle size with a low population (Figure 1a–a3), cannot be detected as a mass loss in TGA. Differently, we started to notice a slight mass loss at 600 °C; in line with TGA, we observed uniform exsolution of larger Pt nanoparticles (Figure 1b–b3). Please note that due to low doping level, less than 1%, and un-reducibility of Al^{3+} cations, we can only observe minor mass change reflecting the Pt exsolution and associated oxygen vacancy formation unlike ferrites or titanates.[45,46]

X-ray diffraction (XRD) patterns of the $LaAlO_3$ and Ba, Pt co-doped $La_{0.9925}Ba_{0.0075}Al_{0.995}Pt_{0.005}O_3$ before and after reduction heat treatment are given in **Figure 2** and refined cell parameters obtained using WinXPOW are listed in **Table 1**. All XRD patterns display (012), (110), (202), (024), (122), (300) and (220) confirming the formation of rhombohedral crystal structure in R-3cH space group (ICSD 182 612) which is the low-temperature stable form of $LaAlO_3$. In this ABO_3 array, La occupies the A-sites with a coordination number of 12 (coordinates twelve oxygen ions) and Al occupies the octahedral sites with a coordination number of 6 (coordinates six oxygen ions). The ionic radii of Al^{3+} and Pt^{4+} in octahedral coordination are 0.675 Å, and 0.765 Å, respectively. Pt is larger than Al but the concentration is very small so this will not give large changes in unit cell parameters. When Pt is reduced to the metallic state, Pt^0, the coordination number is 12 similar to the Pt metal in a face-centred cubic structure (for further discussion see our previous work).[47] In the XRD patterns in unreduced samples, no Pt-related peak is noticeable indicating the successful doping of Pt in the perovskite oxide lattice at 0.5% Pt doping level. However, for doped and reduced samples, we detected peaks of unreacted La_2O_3 as a minority phase (La_2O_3 peaks were indicated by ♦ in Figure 2) which we believe that this phase contributes to the formation of small grains, in line with the previous observation.[48] The presence of the La_2O_3 minority phase can be explained by two possible precursor issues *i)* the hygroscopic nature of La_2O_3 and ii) usage of nonstoichiometric γ-Al_2O_3 precursor. Even if the unreacted γ-Al_2O_3 phase exists in the synthesized material, XRD cannot detect due to its amorphous nature. Additionally, it is worth noting that the sintering

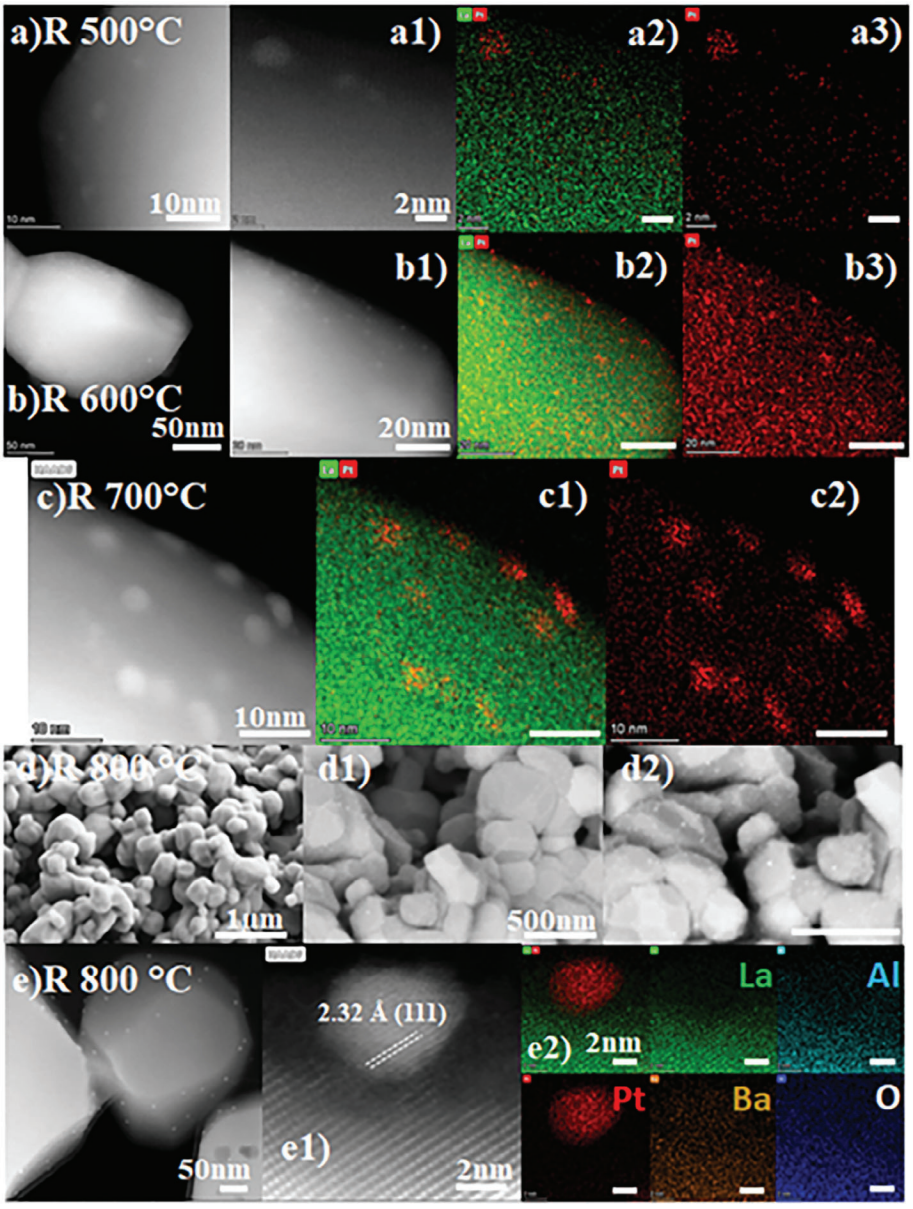

Figure 1. SEM, STEM and STEM-EDS analysis of exsolved Pt nanoparticles from $La_{0.9925}Ba_{0.0075}Al_{0.995}Pt_{0.005}O_3$ between 500 and 800 °C in 5% H_2/N_2 for 12 h. a) HAADF STEM images of exsolved Pt nanoparticles anchored onto 0.5% Pt-LBAO R 500°C reduced at 500 °C. a1-a3) STEM-EDS elemental analysis of exsolved Pt nanoparticle on 0.5% Pt-LBAO R 500 °C (scale bars are 2 nm in a2-a3). b) STEM image and b1-b2) STEM-EDS elemental analysis of exsolved Pt nanoparticle anchored into 0.5% Pt-LBAO R 600°C perovskite oxide (scale bars are 20 nm in b2-b3). c) High-resolution HAADF STEM image and c1-c2) STEM-EDS elemental analysis of exsolved Pt nanoparticle anchored into 0.5% Pt-LBAO R 700 °C perovskite oxide (scale bars are 10 nm in c-c2). d) Low and d1-d2) high magnification SEM images of 0.5% Pt-LBAO R 800 °C showing exsolved Pt nanoparticles after reduction at 800°C. e-e1) High-resolution HAADF STEM images and e2) STEM-EDS elemental analysis of exsolved Pt nanoparticle anchored into 0.5% Pt-LBAO R 800 °C perovskite oxide (scale bars are 2 nm in e2).

temperature of 1200 °C is not sufficient to initiate the full conversion of La_2O_3 and low compared to the temperatures that are mostly used for solid-state reaction synthesis, the sintering conditions require further optimization.

Pt and Ba doping of $LaAlO_3$ induced a slight shift of the main $LaAlO_3$ peak to a lower angle, signifying the expansion of the lattice. In other words, doping treatment of $LaAlO_3$ with Ba and Pt enlarged the unit cell parameters from a = 5.3650(8), c = 13.1303(20), V = 327.30(9) to a = 5.3675(9), c = 13.1381(22), V = 327.80(9), app. 0.15% increase in the cell volume. A minor shift in XRD peak, less than 0.1°, at ≈33.4° after reduction at different temperatures should be explained by considering the combined effect of oxygen vacancy formation, defect formation, and exsolution. We believe that during reduction, the H_2 atmosphere induces oxygen ion loss that leads to oxygen vacancy formation and emergence of Pt nanoparticles. The effects are quite small,

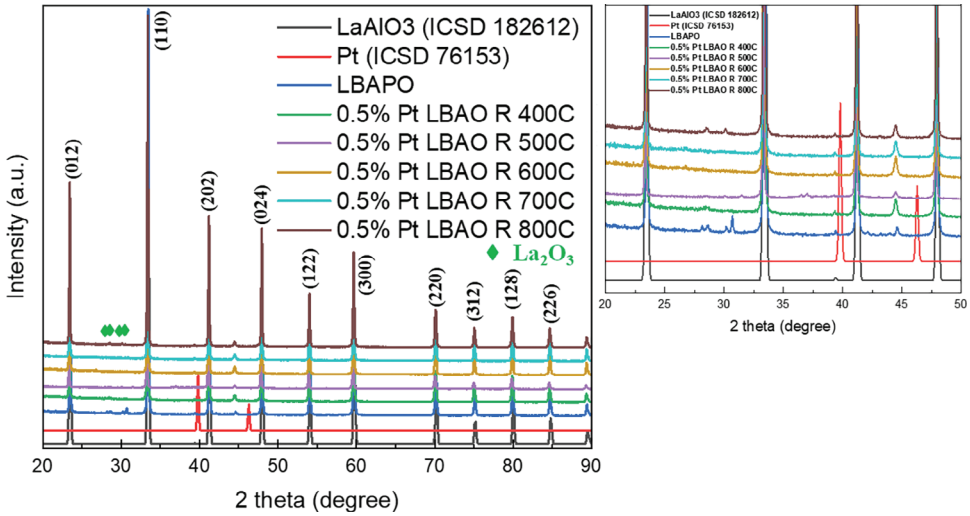

Figure 2. XRD patterns of Pt doped ($La_{0.9925}Ba_{0.0075}Al_{0.995}Pt_{0.005}O_3$) and reduced (0.5% Pt-$La_{0.9925}Ba_{0.0075}Al_{0.995}O_{3-x}$) perovskite oxides between 400 and 800°C for 12 h in 5% H_2/N_2. Inset enlarged image showing the peaks between 20 and 50 °. (The peak at around 44.5° is from the XRD holder).

and further investigations are needed to understand the oxygen vacancy formation and the mechanism of Pt nanoparticle emergence from $LaAlO_3$, that is beyond the scoop of this paper.

Initially, we explored the activity of the catalyst for ORR in O_2-saturated acid solution (0.1 M $HClO_4$) using a rotating ring disc electrode (RRDE) set-up (**Figure 3**; Figure S10, Supporting Information). In the acidic media, ORR onset potentials were 0.4, 0.45, and 0.55 V for 0.5% Pt-LBAO R 500 °C, 0.5% Pt-LBAO R 600 °C and 0.5% Pt-LBAO R 700 °C, respectively. The cyclic voltammetry was recorded at different scan rates (Figure S11, Supporting Information) and the electrochemical surface area (ECSA) values were quantified following Equation 6. According to the findings, the samples reduced at 600 and 800 °C demonstrate the highest ECSA values with 39 and 50. From RRDE profile, we quantified the H_2O_2% and electron transfer number (n) using Equation 7–9, as shown in Figure 3c; Figure S10 (Supporting Information). Accordingly, the average H_2O_2% and n for different samples were over 50% and 2.5-3, indicating the mixed products of H_2O_2 and H_2O (following the reactions 1–2). The lowest activity for two-electron reaction, was observed for the 0.5% Pt-LBAO R 800 °C with 25% H_2O_2 yield and electron transfer number of 3.5 signifying the formation of H_2O as a main reaction product. Additionally, the stability tests were performed by polarizing the electrodes in the mixed region, at 0.7 V versus RHE (Figure 3d). In the polarization curve, the current density dropped to almost zero in the initial stages of the measurement showing the poor stability of the catalyst in an acidic media.

An assessment of samples was carried out in an O_2-saturated alkaline solution (0.1 M KOH), as shown in **Figure 4**. We considered the third linear sweep voltammetry (LSV) cycle of the ORR test as this provides an equilibrated electrode, rather the resultant of high temperature reduction (Figure S12, Supporting Information). The sharp change in ORR activity at ≈0.5 V versus RHE in the first cycle could be explained by the filling of oxygen vacancies, which are one of the main active sites for ORR, with H_2O[49,50] during the initial LSV test. If we evaluate three regions of ORR curves, in the kinetic region (current independent of rotation rate and the reaction rate is limited by the electron transfer from electrocatalyst surface to O_2) the onset potential increased with decreasing reduction temperature. Namely, the highest onset potentials were monitored for the samples reduced at 400 and 500 °C, i.e., 0.89 and 0.97 V (see **Table 2**), respectively. This can indicate reduction at lower temperatures introduces a controlled number of defects and oxygen vacancies significantly improving the conductivity of the perovskite oxide by improving the ionic mobility in perovskite oxides. It is known that in the reduced perovskite oxides, generated oxygen vacancies (V_O) contribute to the bulk conductivity of the perovskite oxide structure [51] and are

Table 1. Refined cell parameters of pristine and reduced perovskite oxide samples.

Samples	a, b [Å]	c [Å]	V [Å^3]
$LaAlO_3$	5.3650[8]	13.1303[20]	327.30[9]
$La_{0.9925}Ba_{0.0075}Al_{0.995}Pt_{0.005}O_3$	5.3675[9]	13.1381[22]	327.80[9]
0.5% Pt-$La_{0.9925}Ba_{0.0075}Al_{0.995}O_{3-\delta}$ 400°C	5.3614[18]	13.1416[13]	327.14[16]
0.5% Pt-$La_{0.9925}Ba_{0.0075}Al_{0.995}O_{3-\delta}$ 500°C	5.3659[10]	13.1343[24]	327.51[11]
0.5% Pt-$La_{0.9925}Ba_{0.0075}Al_{0.995}O_{3-\delta}$ 600°C	5.3657[10]	13.133[3]	327.45[11]
0.5% Pt-$La_{0.9925}Ba_{0.0075}Al_{0.995}O_{3-\delta}$ 700°C	5.3658[11]	13.1324[25]	327.44[11]
0.5% Pt-$La_{0.9925}Ba_{0.0075}Al_{0.995}O_{3-\delta}$ 800°C	5.3621[5]	13.1398[5]	327.19[5]

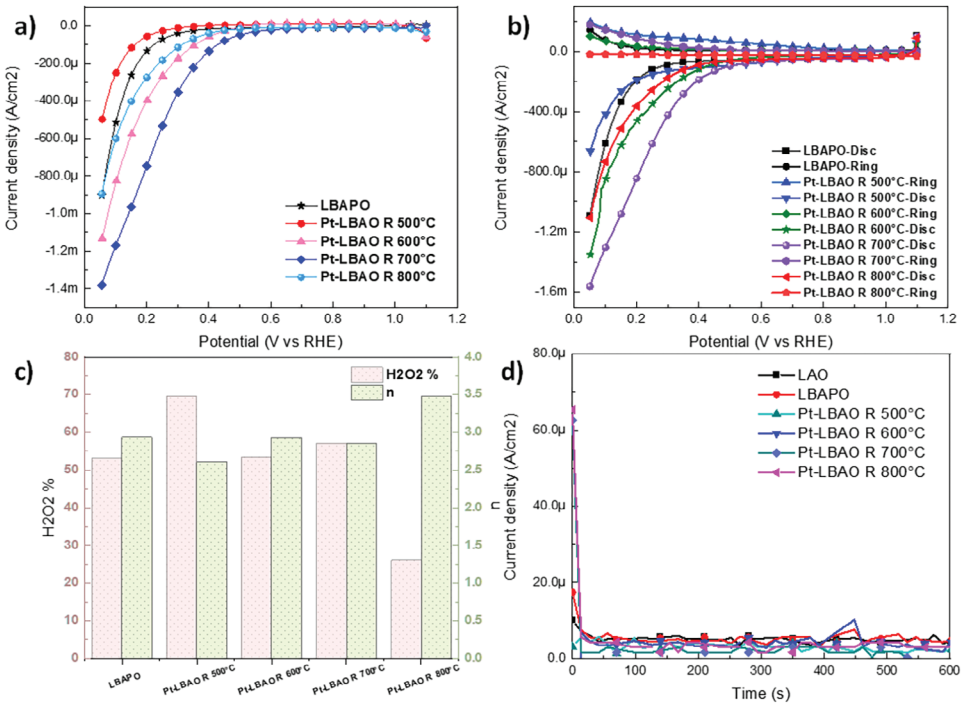

Figure 3. Electrocatalytic ORR tests of LBAPO, 0.5% Pt-LBAO R 500°C, 0.5% Pt-LBAO R 600°C, 0.5% Pt-LBAO R 700 °C and 0.5% Pt-LBAO R 800 °C in 0.1 M $HClO_4$ at 1600 rpm. a) Comparisons of linear sweep voltammetry (LSV) curves measured at 1600 rpm and a scan rate of 10 mV/s, across a potential range of 0.05 to 1.10 V versus RHE. b) Comparisons of rotating ring disc electrode (RRDE) measurements showing disc and ring current densities versus potential at 1600 rpm. c) Bar chart showing the H_2O_2 selectivity and electron transfer number (n) variations at 0.7 V versus RHE. d) Electrochemical stability tests (chronoamperometry, CA) of pristine and reduced perovskite oxides in 0.1 M $HClO_4$ under polarization at 0.7 V versus RHE.

reported as the active sites for ORR.[27] The monitored onset potential for perovskite oxides (0.97 V) is comparable to our commercial reference sample, 1% Pt on C with an onset potential of 1.02 V. A comparable onset potential value illustrates that reducing the sample at lower temperatures enhanced the electronic properties significantly by introducing appropriate/a controlled number of defects and vacancies. In the kinetic-mass controlled mixed region, we observed the same trend, the half-wave potential ($E_{1/2}$) is higher for the samples reduced at lower temperatures, i.e., 0.76 V for 0.5% Pt-LBAO R 500°C and 0.67 V for 0.5% Pt-LBAO R 600 °C, listed in Table 2. In the mass-controlled region (limited by the O_2 diffusion from bulk electrolyte to active site), the limiting current density values at 0.4 V (0.2 V) are higher for the 0.5% Pt-LBAO R 500 °C and 0.5% Pt-LBAO R 600 °C samples, which are ≈2.8 mA cm^{-2} (3.1 mA cm^{-2}) and ≈2.88 mA cm^{-2} (3.1 mA cm^{-2}), respectively. The solubility and diffusivity of oxygen in bulk electrolyte define the limiting current density in the low voltage region. According to Mayrhofer et al. and Walker et al.[52,53] oxygen shows lower solubility and diffusivity in alkaline media than in acidic media, this behaviour results in lower J_{lim} in alkaline media. The Tafel slopes for pristine and reduced perovskite oxides are given in Table 2. Consistent with LSV results, samples reduced at lower temperatures have lower Tafel slopes. On the other hand, with increasing reduction temperature Tafel slopes showed an increasing trend, i.e., 48 mV dec^{-1} for 0.5% Pt-LBAO R 500 °C, 62 mV dec^{-1} for 0.5% Pt-LBAO R 600 °C, and 112 mV dec^{-1} for 0.5% Pt-LBAO R 800 °C samples. This finding suggests lower charge transfer resistance at lower temperatures, and poor charge transfer kinetic for the samples reduced at high temperatures. For the Pt/C reference sample, we measured a Tafel slope of 88 mV dec^{-1}, in line with the research work reporting a Tafel slope of 65–82 mV dec^{-1} for Pt/C in alkaline media.[54] The interpretation of Tafel slope can vary, in other words, some evaluate it as the descriptor of the catalytic activity and some use it to define the rate-determining step. Accordingly, lower Tafel slopes (60 mV dec^{-1}) suggest that the reaction rate is controlled by a pseudo-two-electron reaction and higher values (120 mV dec^{-1}) show that the first electron reduction of oxygen is the rate-determining step.[54–56] Based on this interpretation, reaction rates of 0.5% Pt LBAO R 400 °C, 0.5% Pt LBAO R 500 °C and 0.5% Pt LBAO R 600 °C (with low Tafel slopes) are controlled by a pseudo-two-electron reaction. On the other hand, the reaction rates of 0.5% Pt LBAO R 700 °C and 0.5% Pt LBAO R 800 °C with high Tafel slopes are controlled by electron transfer to the adsorbed oxygen.

The ORR activity was converted to mass activity (see Figure 4b). We monitored a comparable onset potential for perovskite oxide samples to our Pt/C reference sample (0.97 and 1.02 V for 0.5% Pt-LBAO R 500 °C and 1% Pt/C, respectively). The limiting current density values (at 0.4 V) of 4.66 A mg_{Pt}^{-1} (0.5% Pt-LBAO R 500 °C), 4.78 A mg_{Pt}^{-1} (0.5% Pt-LBAO R 600 °C), and 4.63 A mg_{Pt}^{-1} (0.5% Pt-LBAO R 700 °C) are noticeably higher than 2.09 A mg_{Pt}^{-1} value of the Pt/C commercial reference with two times higher Pt content. This finding supports

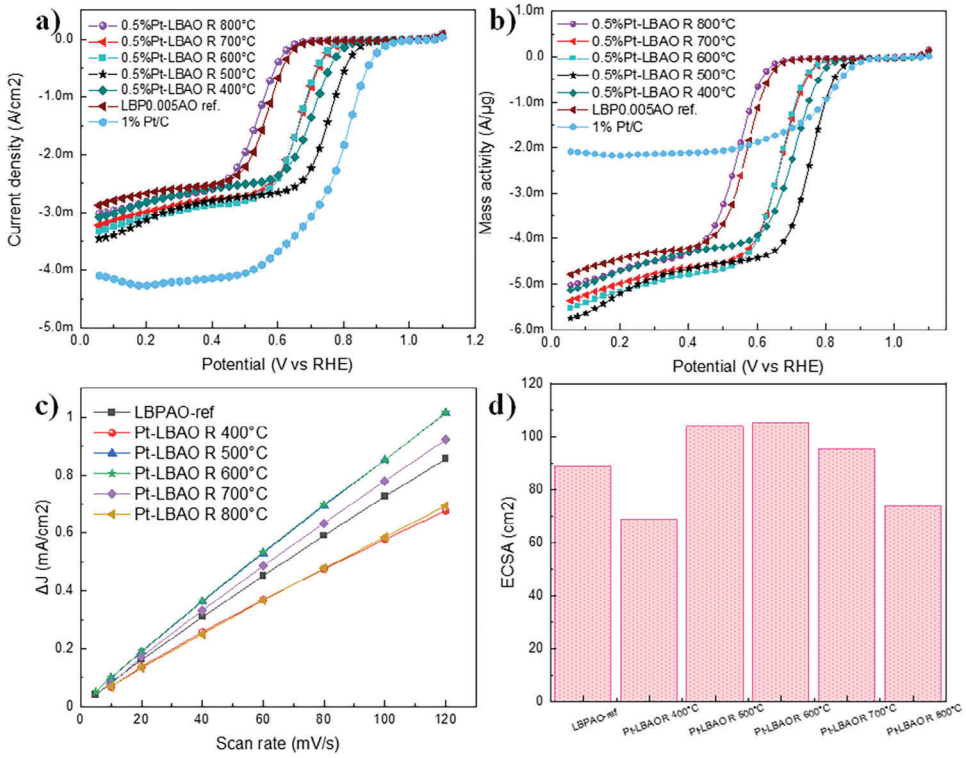

Figure 4. Electrocatalytic ORR tests of $La_{0.9925}Ba_{0.0075}Al_{0.995}Pt_{0.005}O_3$, 0.5% Pt-LBAO R 400°C, 0.5% Pt-LBAO R 500°C, 0.5% Pt-LBAO R 600°C, 0.5% Pt-LBAO R 700°C and 0.5% Pt-LBAO R 800°C measured at 1600 rpm and a scan rate of 10 mV/s in 0.1 M KOH across a potential range of 0.05 to 1.1 V versus RHE. Comparisons of a) specific and b) mass activities of samples. c) Difference between anodic and cathodic current density, $\Delta J = J_A - J_C$, plotted against scan rate. d) Bar chart showing the calculated ECSA values using the slopes of ΔJ versus scan rate plot.

the idea that tuning the intrinsic and extrinsic properties of perovskite oxide enables constructing a highly active catalyst with low Pt loading, 0.59 μg_{Pt} cm^{-2}.

To understand the charge transfer behavior of samples reduced at different temperatures, we performed cyclic voltammetry in $[Fe(CN)_6]^{3-/4-}$ couple, see Figure S13 (Supporting Information). In line with LSV profiles, the increasing reduction temperature decays the monitored current value, and this finding indicates the worsened electrical properties of the material with increasing reduction temperature. We do not observe the contribution of emerged Pt nanoparticles to electrical conductivity since exsolved Pt needs to form a percolation pathway on the substrate for conductivity. According to the current findings, the conductivity of $LaAlO_3$ enhances with the reduction temperature at moderate/mild temperatures due to introducing appropriate amount of V_O, and the conductivity decays after reducing heat treatment at high temperatures. It is worth mentioning that $LaAlO_3$ demonstrate good catalytic activity due its significant acidic character, the conductivity of aluminates will not be systematically affected by reduction-exsolution as other changing factors will have strong influence. Another important parameter, the electrochemical surface area (ECSA), was calculated from non-faradaic current resulting from the adsorption/desorption of ions on the surface calculated using Equation 6 (Figure 4c,d). For this, rotating disc electrode (RDE) voltammetry curves were recorded in non-faradaic region at scan rates between 5 and 120 mV s^{-1}, as

Table 2. Important parameters for the perovskite oxide catalysts in the doped and reduced state in 0.1 M KOH.

Sample	E_{onset} [V]	$E_{1/2}$ [V]	J_{lim} [@ 0.4 V] [mA cm^{-2}]	Tafel slope
1% Pt/C	1.02	0.79	4.14	88
$La_{0.9925}Ba_{0.0075}Al_{0.995}Pt_{0.005}O_3$	0.76	0.58	2.53	120
0.5% Pt-$La_{0.9925}Ba_{0.0075}Al_{0.995}O_{3-\delta}$ 400°C	0.89	0.71	2.58	65
0.5% Pt-$La_{0.9925}Ba_{0.0075}Al_{0.995}O_{3-\delta}$ 500°C	0.97	0.76	2.8	48
0.5% Pt-$La_{0.9925}Ba_{0.0075}Al_{0.995}O_{3-\delta}$ 600°C	0.86	0.67	2.88	62
0.5% Pt-$La_{0.9925}Ba_{0.0075}Al_{0.995}O_{3-\delta}$ 700°C	0.88	0.68	2.79	81
0.5% Pt-$La_{0.9925}Ba_{0.0075}Al_{0.995}O_{3-\delta}$ 800°C	0.74	0.55	2.59	112

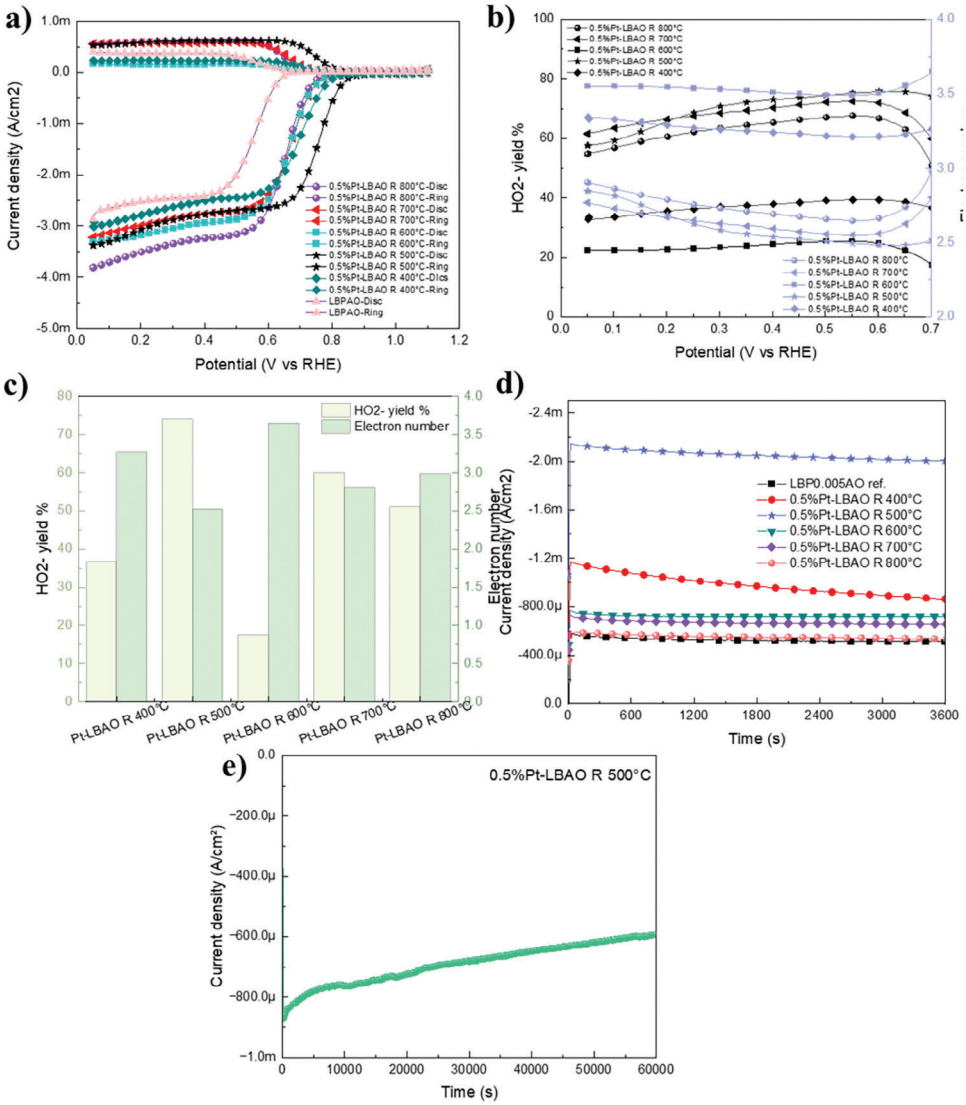

Figure 5. Rotating ring disc electrode voltammogram and stability profiles of LBAPO, 0.5% Pt-LBAO R 400°C, 0.5% Pt-LBAO R 500°C, 0.5% Pt-LBAO R 600°C, 0.5% Pt-LBAO R 700°C and 0.5% Pt-LBAO R 800°C at 1600 rpm in 0.1 M KOH. a) Comparisons of rotating ring disc electrode measurement plots showing disc and ring current densities versus potential. b) Variation of HO_2^- yield % and electron transfer number (n) with applied potential. c) Bar chart showing the comparison of HO_2^- % yield and electron transfer number (n) at 0.7 V versus RHE. d) Electrochemical stability of pristine and reduced perovskite oxides in 0.1 M KOH under polarization at 0.7 V versus RHE. e) Long-term electrocatalytic stability of 0.5% Pt-LBAO R 500°C in 0.1 M KOH under polarization at 0.7 V versus RHE at 1600 rpm.

shown in Figure S14 (Supporting Information). The slope of the $\Delta J = J_A - J_C$ (difference between the anodic current density and the cathodic current density) versus the scan rate graph gives the double-layer capacitance (C_{DL}). We observed the highest slope and the highest electrochemical surface area (ECSA) for the samples reduced at 500 and 600°C. Note that the obtained ECSA values include contributions from active metal sites (exsolved Pt particles), structural defects, and surface defects (oxygen vacancies, strains, cavities), are also influenced by solid-state properties and wettability of the catalyst. Higher active surface area for the samples reduced at lower temperatures is attributed to the lower size (≈2 nm at 600°C) and higher population of exsolved Pt nanoparticles. To estimate $ECSA_{Pt}$, we also attempted to do hydrogen under potential deposition (H_{upd}) measurement and carbon monoxide stripping voltammetry, however, due to low Pt content it was difficult to obtain reliable data (data not shown).

We recorded LSV profiles at varying rotation rates between 100 and 3600 rpm and applied Levich Equation at 0.4 V, illustrated in Figure S15 (Supporting Information). It is noticeable that the current density increased with the rotation rate for all samples and according to the Levich plot, the current increased linearly with the square root of rotation rate (Figure S15e, Supporting Information). The experimental finding illustrates that the reaction rate is controlled by mass transfer at this potential value. To elucidate the reaction mechanism further, we conducted RRDE voltammograms, as given in **Figure 5**a. The electron transfer number (n) and HO_2^- % yield were calculated following Equation 8 and 9 and the plot shows the variation with applied potential, see

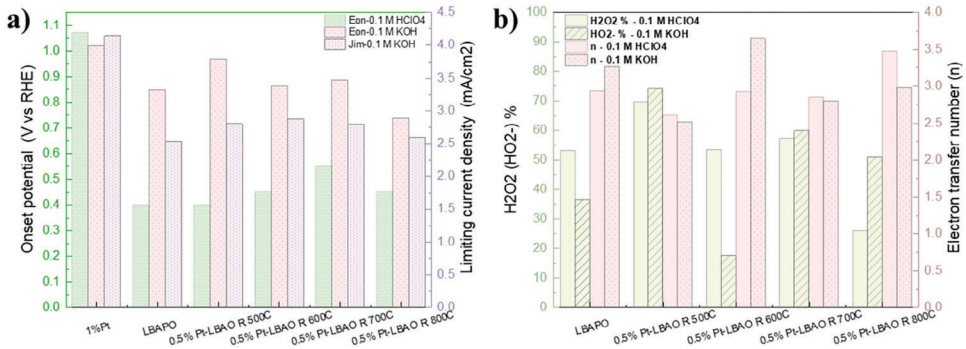

Figure 6. Bar chart showing the comparison of a) onset, half-wave potential and limiting current density and b) H_2O_2 (HO_2^-) and electron transfer number (n) in 0.1 M KOH and 0.1 M $HClO_4$ electrolytes.

Figure 5b. The ORR can occur in either a four-electron pathway (in this desired pathway, O_2 is reduced directly to OH^- product) or a two-electron pathway (adsorbed O_2 is first reduced to OH_2^- and then further reduced to OH^- ion), as described in reactions 4–5. We noticed the highest electron transfer number, 3.8, and the lowest HO_2^- % yield, less than 20%, for the sample reduced at 600 °C (0.7 V mixed region). This demonstrates that the catalyst reduced at 600 °C was more active for a four-electron reaction than a two-electron reaction, resulting in the main reaction product of OH^-. On the other hand, the sample reduced at 500 °C led to over 70% HO_2^- and electron transfer number of ≈2.5, yielding the mixed reaction products of OH^- and HO_2^-. Overall, all samples gave high HO_2^- % yield (over 30%) in alkaline solution. It is known that various parameters, e.g., particle size, electronic structure, crystalline structure, support material type, defect, and crystal grain size have a decisive influence on the reaction path, a two-electron versus a four-electron reactions.[57,58] The reason of high activity for HO_2^- formation in alkaline media is attributed to the dominant outer-sphere electron transfer process (The outer sphere electron transfer predominantly leads to peroxide or peroxide intermediate formation).[59] due to adsorption of OH^- ions that block the O_2 adsorption sites on the catalyst surface. Also, the strength of the interaction between metal and oxygen—strong interaction between oxygen and catalyst may dissociate O_2 with a four-electron reaction, too weak interaction results in dissociation of O_2 with a two-electron reaction, and high selectivity for H_2O_2 or intermediate formation—determine the reaction product.[57] It is necessary to promote inner-sphere electron transfer reaction, which renders a four-electron ORR pathway, by facilitating direct adsorption of molecular oxygen on the active sites.

Another important factor to evaluate the quality of the ORR catalyst is the stability. We analysed it by polarizing the electrodes at 0.7 V versus RHE, as shown in Figure 5d,e. The highest current density at 0.7 V was observed for the sample reduced at 500 °C, followed by the sample treated at 400 °C. This finding also confirms the best improvements in electronic and catalytic properties for the samples reduced at lower temperatures. After the test, the highest degradation in current density noticed for 0.5% Pt-LBAO R 500 °C with 25% drop and other samples exhibited an average 6% decrease. The long-term stability test was performed for the sample reduced at 500 °C, see Figure 5e. In good agreement with the short-term stability test, we monitored max. 30% reduction in the current density. To further analyse the stability of the catalyst, we cycled the sample within different voltage ranges and at different scan rates following the previously reported test conditions,[60] see Figure S17 (Supporting Information). The chronoamperometry (CA) at 0.7 V and accelerated stress tests illustrated that under the present test conditions perovskite oxide-based catalysts show good durability.

The bar charts given in **Figure 6** compare the results of samples tested in acidic and alkaline media. In acidic media, 0.5% Pt-LBAO R 700 °C delivered the highest onset potential of 0.55 V and in basic media, 0.5% Pt-LBAO R 500°C showed the onset potential of 0.97 V which is very close to the onset potential of commercial Pt/C reference sample, 1.02 V (Figure 6a). We monitored higher catalytic activity (higher onset potential), higher ECSA and better electrocatalytic durability in basic media than in acidic media. Furthermore, the catalyst is more active for HO_2^- formation in basic media than in acidic media, attributing to the high activity/affinity to adsorb OH^- ions on $LaAlO_3$ surface, can support the acidic character of the surface—showing tendency to bind OH^- ions preferentially (Figure 6b). The electrocatalytic test results suggests that $LaAlO_3$ based catalyst demonstrated good durability in the alkaline media than in acidic media.

In the literature, Gao et al.[61] reported Pt_3Ni exsolved from 7.5% Pt doped A-site deficient $La_{0.9}Mn_{0.9}Pt_{0.075}Ni_{0.025}O_{3-d}$ perovskite oxide prepared using sol-gel method (reduced at 500°C for 30 min) and investigated for ORR in alkaline media, see Table S1 (Supporting Information) for literature comparision. (Please note that it is difficult to compare the ORR performance of the catalyst reported in this work with the existing literature since methods, catalyst, test conditions and Pt loading differ.) The exsolved Pt_3Ni nanoparticles on reduced $La_{0.9}Mn_{0.9}Pt_{0.075}Ni_{0.025}O_{3-d}$ are ≈20 nm and have a cubic crystal structure. The authors reported the onset potential of 0.92 V and limiting current density of 5.4 mA cm^{-2} at 0.3 V for the Pt loading of 0.015 mg_{Pt} (for 0.4 mg cm^{-2} of catalyst loading) in 0.1 M KOH.[61] Zhao et al. reported onset potential and limiting current density of 1 V and 5.7 mA cm^{-2} (at 0.4 V, Pt loading of 0.121 mg cm^{-2}) for nitrogen doped intermetallic PtNiN on Ketjen black in 0.1 M $HClO_4$.[62] Pt/C reference with 20 wt% Pt (at 14 μg_{Pt} cm^{-2} loading) delivers the ORR onset potential of 1 V versus RHE (J_{lim} is 6 mA cm^{-2} at 0.4 V) in 0.1 M $HClO_4$[63] and 20 wt. % Pt/C (at 25 μg_{Pt} cm^{-2} loading) delivers 1 V versus RHE (J_{lim} is 3.7 mA cm^{-2} at 0.4 V) in 0.1 M KOH[55] (at 5 mV s^{-1}),

respectively. We observed comparable ORR activity with the literature for 0.5 wt% Pt containing $La_{0.9925}Ba_{0.0075}Al_{0.995}Pt_{0.005}O_3$ perovskite oxides at 0.59 μg_{Pt} cm^{-2} Pt loading.

Overall, the ORR activity of the electrocatalyst depends on the electrochemically active sites, surface area, porosity for the optimal mass transfer, and electrical properties of the material. In the perovskite oxides, B-site transition metal and oxygen vacancies are considered to be the active sites. According to the published works, 3–5 nm Pt nanoparticles exhibit the highest reactivity towards ORR due to the effective use of noble metal, utilization, and better catalytic activity.[64–66] In the present work, reducing heat treatment at low temperatures, between 500 and 600 °C, leads to growth of 1–3 nm Pt nanoparticles and introduces an appropriate amount of oxygen vacancies-defects that contribute to electrical conductivity, resulting in higher onset and limiting current density. On the other hand, reducing perovskite oxides at elevated temperatures, e.g., 700–800 °C yields an exsolution of larger nanoparticles, 3–7 nm, introducing oxygen vacancies and causing a sintering effect of grains due to high firing temperature. As a result, we observe lower ORR activity, lower onset potential, and lower current density in the mass-controlled region. We report ORR activity for the electrocatalyst with only 0.5% Pt loading, 0.59 μg_{Pt} cm^{-2} loading with Pt nanoparticle size of 1–7 nm. The U.S. Department of Energy (DOE) target to achieve good catalytic activity, low Pt loading (0.1 mg_{PGM} cm^{-2}), and good durability is to increase the Pt surface area through better dispersions and small particle sizes.[67] Our approach enables the formation of highly dispersed Pt nanoparticles with small particle size at low loadings and delivering good catalytic durability.

3. Conclusion

In this work, we studied the exsolution of Pt nanoparticles from $La_{0.9925}Ba_{0.0075}Al_{0.995}Pt_{0.005}O_3$ with low Pt content and assessed ORR activity as a cathode catalyst at RRDE in acidic and alkaline media. We demonstrated the exsolution of 1–3 nm Pt nanoparticles from $La_{0.9925}Ba_{0.0075}Al_{0.995}Pt_{0.005}O_3$ at low reduction temperature. The exsolved fine Pt nanoparticles from $La_{0.9925}Ba_{0.0075}Al_{0.995}Pt_{0.005}O_3$ obtained during low temperature reduction treatment (600 °C) demonstrated uniform dispersion on perovskite oxide. This configuration enhanced the accessibility of surface Pt atoms and utilization of active nanoparticles during electrocatalytic testing. While catalyst have unsatisfactory activity and durability in acidic media, it exhibited good ORR activity and electrocatalytical stability in basic media. Overall, we believe that this approach will allow designing a perovskite oxide catalyst with minimal noble metal loading for key electrocatalytic reactions, i.e., ORR, OER, and HER.

4. Experimental Section

Sample Preparation and Processing: Technical grade chemicals were used, γ-Al_2O_3 (99.97%, 3 µm) Alfa Aesar, La_2O_3 (99.99%, Sigma Aldrich), $BaCO_3$ (99.8%, Thermo Scientific), PtO_2 (99.95%, Pt 84.4%, Alfa Aeser). As a Pt precursor, house developed $Ba_3Pt_2O_7$ perovskite oxide prepared by solid-state reaction was used, see Figure S1 (Supporting Information). Oxides were dried at different temperatures (Al_2O_3 at 300 °C and La_2O_3 at 800 °C) and weighed while the chemicals were warm. The mixture was mixed with acetone and ≈0.05 wt% Hypermer KD1 dispersant using an ultrasonic Hielscher UP200S probe. The acetone was then evaporated at room temperature under continuous stirring. The mixture was transferred to a crucible and calcined at 1000 °C for 12 h in air. The calcined powder was then ground for 30 min pressed into pellets and fired at 1200 °C for 12 h in O_2 with the flow rate of 100 ml min^{-1} to form the perovskite phase. The prepared pellet was fractured and reduced in 5% H_2/N_2 between 400 and 800 °C for 12 h. Samples investigated in this study were listed in **Table 3**.

Brunauer Emmett and Teller (BET) specific surface area was analyzed by the distribution graph of N_2 adsorption-desorption at 77 K using Micromeritics TRISTAR II 2020. Prior to measurement, the samples were degassed at 200 °C under vacuum overnight using a Quantachrome Flovac degasser (Micromeritics VacPrep 061).

Structural Characterization: To confirm the phase purity and crystallinity, sintered and reduced samples were analyzed by using a PANalytical Empyrean X-ray diffractometer (XRD) operated in reflection mode. The collected XRD data was further analyzed using WinXPOW software. The morphology of the perovskite oxides and exsolved Pt nanoparticles were characterized using JSM-IT800 Schottky Field Emission Scanning Electron Microscope (SEM).

HR-TEM imaging was conducted by the FEI Titan Themis instrument, using a 25 keV He^+ beam with 0.2 pA beam current. The elemental composition was studied by the energy dispersive X-ray (EDX) by spot and mapping analysis to distinguish the Pt nanoparticles on the sample surface compared to the desired perovskite compositions (La, Ba, Pt, Al, and O).

Electrochemical Characterization: The electrochemical activity of the perovskite oxide samples was probed using a rotating ring disc electrode (RRDE) assembly manufactured by Pine Research. The optimized ink composition was 500 µl of 2-propanol, 500 µl of H_2O, 60 µl of Nafion perfluorinated resin solution (5 wt%) from Sigma Aldrich, 6 mg of Pt exsolved perovskite oxide catalyst and 9 mg of carbon powder as a conductive agent. The ink was ultrasonicated for an hour and stirred overnight. The ink (5.5 µl ink, 31 μg_{PO}, 0.14 μg_{Pt} per measurement, 0.2375 cm^2) was drop-casted on a glassy carbon disc and air-dried. The electrochemical performance of the samples was analyzed using linear sweep voltammetry (LSV), rotating ring disc voltammetry (RRDV), and chronoamperometry (CA) at 1600 rpm, at a scan rate of 10 mV s^{-1} between 0.05-1.1 V versus RHE and LSV also recorded at different rotation speeds between 100 and 3600 rpm (all data were collected using sweep from high to low potential values). During RRDV, the Pt ring was polarized at 1.2 V versus RHE to detect the reaction products. For all electrochemical measurements, N_2 was purged in the electrolyte for at least 30 min to eliminate the O_2 in the solution and then O_2 was purged at least for 30 min prior to ORR measurement. The capacitive contribution of the electrode was deduced by subtracting the LSV in N_2 from the LSV profile measured in O_2.

$$E_{(RHE)} = E_{(SCE)} + 0.242 + 0.059\ pH \quad (1)$$

ORR reaction mechanisms in alkaline and acidic media were listed as follows.

In acidic media

$$O_2 + 4H^+ + 4e^- \rightarrow 4H_2O\ (4e^-\ reaction)\ E^\circ = 1.23\ V\ vs\ RHE \quad (2)$$

$$O_2 + 2H^+ + 2e^- \rightarrow H_2O_2\ (2e^-\ reaction)\ E^\circ = 0.70\ V\ vs\ RHE \quad (3)$$

In alkaline media

$$O_2 + 2H_2O + 4e^- \rightarrow 4OH^-\ (4e^-\ reaction)\ E^\circ = 1.23\ V\ vs\ RHE \quad (4)$$

$$O_2 + H_2O + 2e^- \rightarrow HO_2^- + OH^-\ (2e^-\ reaction)\ E^\circ = 0.74V\ vs\ RHE \quad (5)$$

Table 3. Summary of the names, abbreviation and properties of samples prepared and investigated in this work.

Sample name	Formula of the sample	Method	Pt content [wt%]
1% Pt/C	–	Commercial	1
LAO	$LaAlO_3$	Solid-state [ss]	–
LBAPO	$La_{0.9925}Ba_{0.0075}Al_{0.995}Pt_{0.005}O_3$	Solid-state [ss]	0.5
Pt-LBAO R 400°C	0.5% Pt-$La_{0.9925}Ba_{0.0075}Al_{0.995}O_{3-x}$	Solid-state [ss]	0.5
Pt-LBAO R 500°C	0.5% Pt-$La_{0.9925}Ba_{0.0075}Al_{0.995}O_{3-x}$	Solid-state [ss]	0.5
Pt-LBAO R 600°C	0.5% Pt-$La_{0.9925}Ba_{0.0075}Al_{0.995}O_{3-x}$	Solid-state [ss]	0.5
Pt-LBAO R 700°C	0.5% Pt-$La_{0.9925}Ba_{0.0075}Al_{0.995}O_{3-x}$	Solid-state [ss]	0.5
Pt-LBAO R 800°C	0.5% Pt-$La_{0.9925}Ba_{0.0075}Al_{0.995}O_{3-x}$	Solid-state [ss]	0.5

Electrochemical surface area (ECSA) was calculated from the cyclic voltammetry recorded at different scan rates between 5 and 120 mV s^{-1} following the equation.

$$ECSA = \frac{C_{DL}}{2 \times C_S} \tag{6}$$

C_{DL}, double layer capacitance, was a deduced slope of the ΔJ (difference between anodic and cathodic current density) versus scan rate, C_S was 0.04.

The empirical collection efficiency (N) was calculated by measuring the ratio of the ring limiting current (anodic, I_{limr}) to the disk limiting current (cathodic, I_{limd}) at rotation rate of 1600 and 2500 rpm in 10 mM of potassium ferricyanide, $K_3[Fe(CN)_6]$ dissolved in 0.1 M $HClO_4$ at a scan rate of 50 mV s^{-1}. N, n were collection efficiency and electron transfer number, respectively.

$$N = \frac{I_{limr}}{I_{limd}} \tag{7}$$

To quantify the electron transfer number (electron number, n) and produced peroxide or peroxide intermediate yield % (H_2O_2% or HO_2^- %) Equation 8 and 9 were used.

$$H_2O_2\ (HO_2^-)\% = \frac{(200xI_r/N)}{abs\,(I_{limd}) + I_{limr}/N} \tag{8}$$

$$n = \frac{4xabs(I_{limd})}{abs\,(I_{limd}) + I_{limr}/N} \tag{9}$$

The stability of the electrode was evaluated using chronoamperometry by polarizing at 0.7 V (versus RHE) for up to 16 h and accelerated stress tests by cycling the electrode at different potential ranges (0.05-1.5 V versus RHE) and scan rates (200-500 mV s^{-1}) following previous report.[60]

The charge transfer behavior of the samples were compared in 5 mM $K_4Fe[CN]_6$ and 5 mM $K_3Fe[CN]_6$ containing 0.1 M KOH electrolyte at a sweeping rate of 10 mV s^{-1}.

Supporting Information

Supporting Information is available from the Wiley Online Library or from the author.

Acknowledgements

The authors acknowledge support from the Engineering and Physical Sciences Research Council (EPSRC) for Critical Mass Grant EP/R023522/1, Light element Analysis Facility Grant EP/T019298/1, the Strategic Equipment Resource Grant EP/R023751/1 and UK-HyRES: Hub for Research Grant EP/X038963/1.

Conflict of Interest

The authors declare no conflict of interest.

Data Availability Statement

The research data underpinning this publication can be accessed at https://doi.org/10.17630/c4f400d7-57b7-4dff-bad8-9c54943c5b3c.[68]

Keywords

alkaline fuel cells, electrocatalyst, $LaAlO_3$, oxygen reduction reaction, ORR, perovskite oxides, Pt exsolution

Received: September 10, 2023
Revised: January 11, 2024
Published online:

[1] H. A. Firouzjaie, W. E. Mustain, *ACS Catal.* **2020**, *10*, 225.
[2] S. Cherevko, N. Kulyk, K. J. J. Mayrhofer, *Nano Energy* **2016**, *29*, 275.
[3] I. E. L. Stephens, A. S. Bondarenko, U. Grønbjerg, J. Rossmeisl, I. Chorkendorff, *Energy Environ. Sci.* **2012**, *5*, 6744.
[4] B. Fang, N. K. Chaudhari, M.-S. Kim, J. H. Kim, J.-S. Yu, *J. Am. Chem. Soc.* **2009**, *131*, 15330.
[5] F. Bíró, G. Z. Radnóczi, M. Takács, Z. Baji, C. Dücső, I. Bársony, *Procedia Eng* **2016**, *168*, 1148.
[6] S. Ozkan, F. Valle, A. Mazare, I. Hwang, N. Taccardi, R. Zazpe, J. M. Macak, I. Cerri, P. Schmuki, *ACS Appl. Nano Mater.* **2020**, *3*, 4157.
[7] J. Zhang, C. Chen, S. Chen, Q. Hu, Z. Gao, Y. Li, Y. Qin, *Catal. Sci. Technol.* **2017**, *7*, 322.
[8] X. Tian, X. F. Lu, B. Y. Xia, X. W. (David) Lou, *Joule* **2020**, *4*, 45.
[9] L. Zhao, J. Zhu, Y. Zheng, M. Xiao, R. Gao, Z. Zhang, G. Wen, H. Dou, Y. Deng, A. Yu, Z. Wang, Z. Chen, *Adv. Energy Mater.* **2022**, *12*, 2102665.
[10] R. L. Borup, A. Kusoglu, K. C. Neyerlin, R. Mukundan, R. K. Ahluwalia, D. A. Cullen, K. L. More, A. Z. Weber, D. J. Myers, *Curr. Opin. Electrochem.* **2020**, *21*, 192.
[11] J. Irvine, J. L. M. Rupp, G. Liu, X. Xu, S. Haile, X. Qian, A. Snyder, R. Freer, D. Ekren, S. Skinner, O. Celikbilek, S. Chen, S. Tao, T. H. Shin, R. O'Hayre, J. Huang, C. Duan, M. Papac, S. Li, V. Celorrio, A. Russell, B. Hayden, H. Nolan, X. Huang, G. Wang, I. Metcalfe, D. Neagu, S. G. Martín, *J. Phys. Energy* **2021**, *3*, 031502.
[12] H. J. Muñoz, S. A. Korili, A. Gil, *Materials (Basel)* **2022**, *15*, 3288.
[13] Q. N. Tran, O. Gimello, N. Tanchoux, M. Ceretti, S. Albonetti, W. Paulus, B. Bonelli, F. Di Renzo, *Catalysts* **2021**, *11*, 344.

[14] H. Imai, T. Tagawa, *J. Chem. Soc. Chem. Commun.* **1986**, *1*, 52.
[15] H. Wang, L. Zhang, C. Hu, X. Wang, L. Lyu, G. Sheng, *Chem. Eng. J.* **2018**, *332*, 572.
[16] D. Mukai, Y. Murai, T. Higo, S. Ogo, Y. Sugiura, Y. Sekine, *Appl. Catal. A Gen.* **2014**, *471*, 157.
[17] Y. Deng, K. Zhang, Y. Yang, X. Shi, L. Yang, W. Yang, Y. Wang, Z.-G. Chen, *J. Alloys Compd.* **2019**, *774*, 434.
[18] E. B. Shaik, S. K. S. S. Pindiprolu, C. S. Phanikumar, T. Samuel, B. V. N. Kumar, P. M. Santhoshi, P. V. S. S. S. N. Reddy, P. Kumar B, R. K. Ramachandra, *Opt. Mater. (Amst)*. **2020**, *107*, 110162.
[19] A. Sato, S. Ogo, Y. Takeno, K. Takise, J. G. Seo, Y. Sekine, *ACS Omega* **2019**, *4*, 10438.
[20] D. Mukai, Y. Izutsu, Y. Sekine, *Appl. Catal. A Gen.* **2013**, *458*, 71.
[21] T. Yabe, Y. Kamite, K. Sugiura, S. Ogo, Y. Sekine, *J. CO2 Util.* **2017**, *20*, 156.
[22] Sandeep, D. P. R., A. Shankar, M. P. Ghimire, R. Khenata, R. K. Thapa, *J. Magn. Magn. Mater.* **2016**, *417*, 313.
[23] A. Hernández Martínez, E. Lopez, S. Larrégola, O. Furlong, M. S. Nazzarro, L. E. Cadús, F. N. Agüero, *Mater. Today Chem.* **2022**, *26*, 101077.
[24] R. Ianoş, R. Lazău, R. Băbuţă, E. Muntean, E.-A. Moacă, C. Păcurariu, *Dye. Pigment.* **2018**, *155*, 218.
[25] C. Anil, J. M. Modak, G. Madras, *Mol. Catal.* **2020**, *484*, 110805.
[26] T. H. T. Nguyen, M. Dokiya, S. Wang, H. Tagawa, T. Hashimoto, *Solid State Ionics* **2000**, *130*, 229.
[27] Q. Ji, L. Bi, J. Zhang, H. Cao, X. S. Zhao, *Energy Environ. Sci.* **2020**, *13*, 1408.
[28] Y. Matsumoto, H. Yoneyama, H. Tamura, *Bull. Chem. Soc. Jpn.* **1978**, *51*, 1927.
[29] D. Neagu, G. Tsekouras, D. N. Miller, H. Ménard, J. T. S. Irvine, *Nat. Chem.* **2013**, *5*, 916.
[30] D. Neagu, V. Kyriakou, I.-L. Roiban, M. Aouine, C. Tang, A. Caravaca, K. Kousi, I. Schreur-Piet, I. S. Metcalfe, P. Vernoux, M. C. M. van de Sanden, M. N. Tsampas, *ACS Nano* **2019**, *13*, 12996.
[31] D. Neagu, E. I. Papaioannou, W. K. W. Ramli, D. N. Miller, B. J. Murdoch, H. Ménard, A. Umar, A. J. Barlow, P. J. Cumpson, J. T. S. Irvine, I. S. Metcalfe, *Nat. Commun.* **2017**, *8*, 1855.
[32] H. Tanaka, M. Uenishi, M. Taniguchi, I. Tan, K. Narita, M. Kimura, K. Kaneko, Y. Nishihata, J. Mizuki, *Catal. Today* **2006**, *117*, 321.
[33] M. Taniguchi, H. Tanaka, M. Uenishi, I. Tan, Y. Nishihata, J. Mizuki, H. Suzuki, K. Narita, A. Hirai, M. Kimura, *Top. Catal.* **2007**, *42*, 367.
[34] M. A. Naeem, D. B. Burueva, P. M. Abdala, N. S. Bushkov, D. Stoian, A. V. Bukhtiyarov, I. P. Prosvirin, V. I. Bukhtiyarov, K. V. Kovtunov, I. V. Koptyug, A. Fedorov, C. R. Müller, *J. Phys. Chem. C* **2020**, *124*, 25299.
[35] V. Kyriakou, D. Neagu, G. Zafeiropoulos, R. K. Sharma, C. Tang, K. Kousi, I. S. Metcalfe, M. C. M. van de Sanden, M. N. Tsampas, *ACS Catal.* **2020**, *10*, 1278.
[36] L. Lindenthal, R. Rameshan, H. Summerer, T. Ruh, J. Popovic, A. Nenning, S. Löffler, A. K. Opitz, P. Blaha, C. Rameshan, *Catalysts* **2020**, *10*, 268.
[37] K.-S. Wang, J.-F. Tan, P. Hu, Z.-T. Yu, F. Yang, B.-L. Hu, R. Song, H.-C. He, A. A. Volinsky, *Mater. Sci. Eng. A* **2015**, *636*, 415.
[38] Y. Zhao, L. Xu, M. Guo, Z. Li, Z. Xu, J. Ye, W. Li, S. Wei, *J. Mater. Res. Technol.* **2022**, *19*, 4003.
[39] V. Kulyk, Z. Duriagina, A. Kostryzhev, B. Vasyliv, V. Vavrukh, O. Marenych, *Materials (Basel)* **2022**, *15*, 5212.
[40] I. Mahmud, M.-S. Yoon, I.-H. Kim, M.-K. Choi, S.-C. Ur, *J. Korean Phys. Soc.* **2016**, *68*, 35.
[41] Z. Dong, N. Liu, Z. Ma, C. Liu, Q. Guo, Y. Liu, *J. Alloys Compd.* **2017**, *695*, 2969.
[42] M. Q. Jun-jun Yang, G. Chen, Z. Chen, X.-d. Mu, Y. Yu, L. Zhang, X. Li, X. Qu, *Trans. Nonferrous Met. Soc. China* **2020**, *30*, 3296.
[43] B. Brahmaroutu, G. L. Messing, S. Trolier-McKinstry, *J. Mater. Sci.* **2000**, *35*, 5673.
[44] S.-Y. Chung, D. Y. Yoon, S.-J. L. Kang, *Acta Mater.* **2002**, *50*, 3361.
[45] A. P. Panunzi, L. Duranti, I. Luisetto, N. Lisi, M. Marelli, E. Di Bartolomeo, *Chem. Eng. J.* **2023**, *471*, 144448.
[46] D. Neagu, J. T. S. Irvine, *Chem. Mater.* **2011**, *23*, 1607.
[47] M. Kothari, Y. Jeon, D. N. Miller, A. E. Pascui, J. Kilmartin, D. Wails, S. Ramos, A. Chadwick, J. T. S. Irvine, *Nat. Chem.* **2021**, *13*, 677.
[48] D. Mukai, S. Tochiya, Y. Murai, M. Imori, T. Hashimoto, Y. Sugiura, Y. Sekine, *Appl. Catal. A Gen.* **2013**, *453*, 60.
[49] A. V. Virkar, H.-D. Baek, *J. Am. Ceram. Soc.* **2004**, *85*, 3059.
[50] H. Qi, Y.-L. Lee, T. Yang, W. Li, W. Li, L. Ma, S. Hu, Y. Duan, G. A. Hackett, X. Liu, *ACS Catal.* **2020**, *10*, 5567.
[51] M. Risch, *Catalysts* **2017**, *7*, 154.
[52] M. Schalenbach, A. R. Zeradjanin, O. Kasian, S. Cherevko, K. J. J. Mayrhofer, *Int. J. Electrochem. Sci.* **2018**, *13*, 1173.
[53] K. E. Gubbins, R. D. Walker, *J. Electrochem. Soc.* **1965**, *112*, 469.
[54] T. Shinagawa, A. T. Garcia-Esparza, K. Takanabe, *Sci. Rep.* **2015**, *5*, 13801.
[55] R. Zeng, Y. Yang, X. Feng, H. Li, L. M. Gibbs, F. J. DiSalvo, H. D. Abruña, *Sci. Adv.* **2022**, *8*, 35.
[56] X. Ge, A. Sumboja, D. Wuu, T. An, B. Li, F. W. T. Goh, T. S. A. Hor, Y. Zong, Z. Liu, *ACS Catal.* **2015**, *5*, 4643.
[57] N. Wang, S. Ma, P. Zuo, J. Duan, B. Hou, *Adv. Sci.* **2021**, *8*, 2100076.
[58] S. Siahrostami, A. Verdaguer-Casadevall, M. Karamad, D. Deiana, P. Malacrida, B. Wickman, M. Escudero-Escribano, E. A. Paoli, R. Frydendal, T. W. Hansen, I. Chorkendorff, I. E. L. Stephens, J. Rossmeisl, *Nat. Mater.* **2013**, *12*, 1137.
[59] N. Ramaswamy, S. Mukerjee, *J. Phys. Chem. C* **2011**, *115*, 18015.
[60] E. Pizzutilo, S. Geiger, J.-P. Grote, A. Mingers, K. J. J. Mayrhofer, M. Arenz, S. Cherevko, *J. Electrochem. Soc.* **2016**, *163*, F1510.
[61] Y. Gao, J. Wang, Y. Q. Lyu, K. Lam, F. Ciucci, *J. Mater. Chem. A* **2017**, *5*, 6399.
[62] X. Zhao, C. Xi, R. Zhang, L. Song, C. Wang, J. S. Spendelow, A. I. Frenkel, J. Yang, H. L. Xin, K. Sasaki, *ACS Catal.* **2020**, *10*, 10637.
[63] H. A. Gasteiger, S. S. Kocha, B. Sompalli, F. T. Wagner, *Appl. Catal. B Environ.* **2005**, *56*, 9.
[64] Y. Takasu, N. Ohashi, X.-G. Zhang, Y. Murakami, H. Minagawa, S. Sato, K. Yahikozawa, *Electrochim. Acta* **1996**, *41*, 2595.
[65] J. C. Meier, C. Galeano, I. Katsounaros, J. Witte, H. J. Bongard, A. A. Topalov, C. Baldizzone, S. Mezzavilla, F. Schüth, K. J. J. Mayrhofer, *Beilstein J. Nanotechnol.* **2014**, *5*, 44.
[66] M. Nesselberger, S. Ashton, J. C. Meier, I. Katsounaros, K. J. J. Mayrhofer, M. Arenz, *J. Am. Chem. Soc.* **2011**, *133*, 17428.
[67] Fuel Cell Technical Team Roadmap, **2017**.
[68] S. Ozkan, S. J. Kim, D. N. Miller, J. T. S. Irvine, Dataset. University of St Andrews Research Portal. 2024, https://doi.org/10.17630/c4f400d7-57b7-4dff-bad8-9c54943c5b3c.